Türker, E., Cotton, F., Pilz, M., Weatherill, G. (2022): Analysis of the 2019 Mw 5.8 Silivri Earthquake Ground Motions: Evidence of Systematic Azimuthal Variations Associated with Directivity Effects. - Seismological Research Letters, 93, 2A, 693-705.

https://doi.org/10.1785/0220210168

Analysis of the 2019 M_W5.8 Silivri Earthquake ground motions: Evidence of systematic azimuthal variations associated with directivity effects.

Elif Türker[*1,2], Fabrice Cotton[1,2], Marco Pilz[1], Graeme Weatherill[1]

[1] Helmholtz Centre Potsdam, GFZ German Research Centre for Geosciences, Potsdam, Germany

[2] University of Potsdam, Institute of Geosciences, Potsdam, Germany

***Corresponding author:** etuerker@gfz-potsdam.de

Abstract

The Main Marmara Fault (MMF) extends for 150 km through the Sea of Marmara and forms the only portion of the North Anatolian Fault Zone that has not ruptured in a large event (M_W > 7) for the last 250 years. Accordingly, this portion is potentially a major source contributing to the seismic hazard of the Istanbul region. On 26 September 2019, a sequence of moderate-sized events started along the MMF only 20 km south of Istanbul and were widely felt by the population. The largest three events, M_W 5.8 (26th September at 10:59 UTC), M_W 4.1 (26th September 2019, 11:26 UTC), and M_W 4.7 (20th January 2020) were recorded by numerous strong-motion seismic stations and the resulting ground motions were compared to the predicted means resulting from a set of the most recent ground motion prediction equations (GMPEs). The estimated residuals were used to investigate the spatial variation of ground

motion across the Marmara Region. Our results show a strong azimuthal trend in ground motion residuals, which might indicate systematically repeating directivity effects towards the Eastern Marmara Region.

Introduction

On 26 September 2019 the Marmara Region was struck by two moderate-sized events with magnitudes M_W 5.8 (at 10:56 AM UTC, Event 1) and M_W 4.1 (at 11:27 AM UTC, Event 2). A few months later on 11 January 2020, a M_W 4.7 event (Event 3) occurred 5 km from the two preceding events (in the following, the three earthquakes are termed the Silivri Sequence). This sequence of earthquakes produced the largest ground motions recorded in the Marmara Region since 20 years (after the two destructive M_W 7.4 and M_W 7.2 Kocaeli and Düzce events, respectively, in 1999). The location of these events is suggested to represent the transition point between the creeping Central Basin (CeB) and the locked Kumburgaz Basin (KB) (see Figure 1) located on the western and eastern edges of the Main Marmara Fault (MMF), respectively (Bohnhoff et al., 2013, 2017; Ergintav et al., 2014; Schmittbuhl et al., 2016). The MMF represents the only portion of the North Anatolian Fault Zone (NAFZ), a 1600 km long dextral strike-slip fault that crosses northern Turkey, which has not ruptured in a large (+M_W 7) event for the last 250 years. With an estimated recurrence interval of 250-300 years, this section poses the greatest seismic hazard and risk for the whole Marmara Region, especially for metropolitan Istanbul, which is only 20 km north of the MMF and is home to more than 15,000,000 people (Erdik et al., 2003; Parsons, 2004; Hergert and Heidbach, 2010; Murru et al., 2016). Although no loss of life was reported as a result of the Silivri Sequence, and the magnitude of the events was not large, their critical location on the creep-locked transition point and the fact that the area has not experienced any significant ruptures for the last 20 years provides the motivation to analyze the sequence's physical characteristics in terms of the spatial-temporal evolution of the resulting seismicity and to resolve a detailed rupture geometry (Durand et al., 2020; Karabulut et al., 2021). For example, the study of Karabulut et al. (2021) analyzed the fore- and aftershock activity of the Silivri Sequence and concluded that there was eastward rupture propagation, with an increase of stress rates along a 10 km length of the eastern MMF (CeB and KB) and an 8 km long rupture with directivity towards the east, posing an increased level of seismic hazard for the Istanbul region.

We take advantage of the spatially well-distributed strong ground motion stations operated by the Disaster and Emergency Management Authority of Turkey (AFAD) and use the large number of stations (182) that have recorded this sequence to examine the regional variability of ground motion amplitudes for intensity measures such as Peak Ground Acceleration (PGA) and Peak Spectral Acceleration (PSA) at different spectral periods. The evaluation of ground motion variability is undertaken by calculating the residuals, which are defined as the difference between the observed (recorded) data and those predicted by the most recent ground motion prediction equations (GMPEs). When the variability is decomposed into path-, site- and source-effects, our results suggest that the Silivri Sequence produced ground motions with a systematically strong dependency on the source-to-site azimuth that could not be captured by recent GMPEs.

Strong ground motion database

We used the processed (0.1-25 Hz Butterworth bandpass filtered, detrended, and mean removed) strong ground motion records of the Silivri earthquake sequence, the specific seismological properties of which are listed in Table 1. The records were gathered from the New Turkish Accelerometric Database and Analysis System launched by the Disaster and Emergency Management Authority of Turkey (AFAD-TADAS). The provided recordings' continuous and template waveforms were detrended and filtered between 1 and 25 Hz using a second- order Butterworth band-pass filter before further processing. The selected earthquakes are all located along the Main Marmara Fault (MMF) segment with epicentral distances of less than 5 km from each other. Figure 1 shows the locations of the three events and the stations that provided the recorded PGA values of the M_W5.8 mainshock. The stations are in general azimuthally well-distributed, however, there are more stations around the Armutlu Peninsula in the Eastern Marmara towards Kocaeli, which experienced major damage during the 1999 event. The maximum level of ground motion shows remarkable azimuthal variability with greater PGA values north and east of the epicenter and significantly lower PGA values towards the west. The general pattern of this spatial variation is independent of the stations' site class and remains stable for other spectral periods up to 2s (see supplementary material). However, this distribution will be analyzed in detail in the following sections. For the comparison of the results with existing GMPEs, only ground motion recordings from free-field stations with source-to-site distances of less than 200 km were used, ensuring that the distance is within the validity range of the selected GMPEs. The Joyner-Boore-Distance, R_{JB}, (the closest distance from the surface projection of the fault rupture plane to the recording site) was selected as the reference distance measure since the selected ground motion models (except for Chiou and Youngs, 2014) are using this reference distance metric. R_{JB} values for the M_W 5.8 event have been taken from the AFAD-TADAS database (last accessed June 2020). For the M_W < 5 events, R_{JB}values were not available, so we assumed $R_{JB} = R_{epi}$ since the fault plane for these earthquakes is small and the extended source-to-site distance metrics can be compared with point-source distance measures such as R_{epi} (Ambraseys et al., 2005). Records from sites with unknown or inferred v_{S30} (averaged shear-wave velocity of the upper-most 30 m) values have been discarded and only those with measured v_{S30} values are used in the analysis. The sites have v_{S30} values ranging from 181 m/s to 1747 m/s with a median v_{S30} of 352 m/s. Therefore, 238 records (out of 286) from 182 stations were used to evaluate the applicability of a set of recent reference GMPEs that will be discussed in the following section.

[Table 1]

Methods

Comparison with ground motion prediction equations (GMPEs)

Ground motion prediction equations describe the distribution of ground motion by a median and logarithmic standard deviation (Strasser et al., 2009). A general and simplified form of empirical GMPEs is given by equation 1 (Al Atik et al., 2010).

$$Y = f(X_{es}, \theta) + \Delta \quad (1)$$

Here, the term $f(X_{es}, \theta)$ describes the ground motion model itself, with X_{es} representing the explanatory variables (such as magnitude, source-to-site distance, faulting mechanism, and site-descriptor parameters), and θ representing the vector of the coefficients derived using statistical regression analysis. The latter term Δ refers to the total variability of the ground motion – described by a normal distribution with a mean of 0 and standard deviation, σ, and will be discussed in the next section. Y is the natural logarithm of the observed ground motion intensity measures, such as PGA, PGV (Peak Ground Velocity), and PSA for different periods. Here, we first analyze the residuals in the form of histogram plots (Figure 2) and assess the performance of the reference GMPEs with respect to the Silivri Sequence (observed data). The pre-selection phase for defining a set of reference GMPEs that could appropriately represent the target area is based on the studies of Cotton et al. (2006) and Bommer et al. (2010), who defined the exclusion criteria for GMPEs for specific target regions. These are briefly: 1) the model is from an irrelevant tectonic regime, 2) the model is not published in a peer-reviewed journal, 3) the dataset and the ground motion model are insufficiently documented, 4) the GMPE has been updated by a more recent model, 5) the frequency range of the GMPE is not appropriate for the use of engineering applications, 6) the functional form of the model is inappropriate, and 7) the regression coefficients or the regression model are judged to be inappropriate.

Following the application of these criteria, the observed ground motion amplitudes are compared against six GMPEs: one local GMPE (Kale et al., 2015), three pan-European GMPEs (Akkar et al., 2014; Bindi et al., 2014; Kotha et al., 2020), and two global GMPEs (Boore et al., 2014; Chiou and Youngs, 2014), which are abbreviated from hereon as Ka15, ASB14, Bi14, Ko20, BSSA14, and CY14, respectively. The key properties of these six GMPEs and their underlying data sets are presented in Table 2. The NGA-W2 models CY14 and BSSA14 require the depth-to-bedrock parameter $z_{1.0}$, which is not reported for these stations. Accordingly, the values of $z_{1.0}$ were estimated using the empirical relationship between v_{S30} and $z_{1.0}$ (Chiou and Youngs, 2014). Figure 2 shows the PGA within-event residuals, which are based on the mixed-effect regression proposed by Bates (2015). The mixed-effects regression model includes a fixed-effect and random-effects part, whereas the former is represented by the explanatory variables in the GMPE, such as magnitude, distance and v_{S30}, and the latter random-effects are the site- and source parameters. Accordingly, the selected ground motion models predict, without major discrepancies, the observations as indicated by the close agreement of the mean and the variability of the residuals.

This consistency is still apparent for periods up to 3 s when considering the PSA. Accordingly, the analysis is robust with respect to the choice of GMPEs; hence, we will proceed with the model of Bindi et al. (2014), which gives a marginally better fit shown by the overlapping residual curves in Figure 2.

[Figure 2 here]

[Table 2 on a separate page]

Between- and within-event residual analysis

The total residual of the ground motion model (Δ in Equation 1) is subdivided into the between-event (δB_e) and within-event (δW_{es}) components (Al Atik et al., 2010) in order to analyze source-, path-, and site effects that are not accounted for by the parameters in the ground motion models themselves, and thus contribute to variability that arises with the use of these ground motion prediction equations. δB_e describes the average shift of the observed ground motion resulting from an earthquake (*e*) from the median calculated using the GMPE. The misfit between an individual station recording (*s*) and the earthquake-specific (*e*) median predicted by the model is called the within-event variability, δW_{es}. The between-event residuals quantify the remaining source-effects that are not captured by the source parameters included in the GMPEs, while the within-event residuals represent azimuthal differences in source-, path- and site-effects that are not captured by the path- and site descriptor parameters. δB_e and δW_{es} are normally distributed, uncorrelated random variables with zero means and standard deviations of τ and ϕ, respectively. Accordingly, σ can be described by equation 2:

$$\sigma = \sqrt{(\tau^2 + \phi^2)} \tag{2}$$

The GMPE represents a good with the data, if the normalized residuals match to a normal standard distribution (Scherbaum et al, 2004). The normalized between-event residuals for the three earthquakes are estimated using a random effects modelling approach (Bates et al., 2015) for periods up to PSA = 3 s (Figure 3). The 26 September 2019 M_W 4.1 (Event 2) and 20 January 2020 M_W 4.7 (Event 3) events show positive between-event residuals (e.g., ground-shaking), indicating that the observed shaking is higher than that predicted by the median of the GMPE, although well within the variability range of $\pm 1\sigma$ that is expected from a normal distribution. The M_W 5.8 mainshock shows the opposite trend, with negative between-event residuals for most periods. This observation of higher between-event residuals for the aftershocks than for the mainshock contrasts with recent studies, such as Bindi et al. (2019), which have shown that aftershocks usually display lower between-events residuals than those of the mainshock, implying lower stress drop and, thus, lower than expected shaking. This does not appear to be the case during the Silivri Sequence.

[Figure 3 here]

The δW_{es} residuals for all events were calculated for PGA and PSA periods between 0.01s and 2.0 s (but only the results for PGA are presented in this paper). The within-event residuals against R_{JB} and v_{S30} are shown in Figure 4, whereby the stations are colored with respect to their source-to-site longitudinal location. The red zero line indicates that there is no discernible bias with respect to the selected GMPEs.

[Figure 4 here]

For distances less than $R_{JB} < 50$ km, the observed values are lower than the predicted medians. We note, however, that the number of near-fault stations (distances < 80 km) is comparatively small. For larger distances ($R_{JB} > 50$ km) there is no trend with distance at any period. A comparison with the site descriptor parameter, v_{S30}, shows an almost equal distribution of ground motion residuals, thus both comparisons confirm that the ground motion models are largely unbiased with respect to v_{S30} or R_{JB}.

Azimuthal variations in within-event residuals

The noticeable trend in the spatial distribution of the recorded PGA with increasing values towards the northern and eastern Marmara (as shown in Figure 1) will be analyzed in this section. The calculated residuals shown in Figure 4 demonstrate how the within-event residuals are strongly dependent on the longitudinal position of the recording stations relative to the epicenters. Figure 5a-c shows these normalized residuals using the Bi14 model as a function of the stations' locations for PGA and all three events separately. Again, we show only the PGA because here the trend is most pronounced, although the trend itself persists for other periods of spectral acceleration. The reader is referred to the supplement of this paper for the results over the entire frequency range. A clear regional (azimuthal) trend in ground motion residuals can be observed for stations that are located towards the rupture propagation (i.e., the eastward of the epicenters). Here, the observed ground motion amplitudes are systematically higher than zero. By contrast, those ground motions that arrive at stations away from the direction of rupture propagation (westward from the epicenter) show a clear negative trend with respect to the reference GMPE of Bi14. This confirms that the ground motion recorded along the Asian part of Istanbul and northeast of the Armutlu Peninsula towards Kocaeli (i.e., the Eastern Marmara Region) is noticeably higher than ground motion in the Western Marmara Region. However, the number of recorded stations is lower for the M_W 4.1 aftershock (Figure 5b), making the trend less pronounced.

[Figure 5 here]

For the M_W 5.8 event (Figure 5a) the stations in Western Marmara are spatially well distributed and the region is well covered by seismic stations, hence, an increasing number of seismic observations would most likely not change the overall trends. The azimuthal trend is systematically repeating even for the smaller events and does not vanish with increasing period. To understand the potential threat of these systematic higher ground motion levels in specific parts of the Marmara Region, we next examine the site-, path-, and source effects that could influence ground motion variability. This trend is apparent, regardless of the GMPE chosen, and confirms the study of Karabulut et al. (2021) who proposed an eastward propagation of the rupture (in combination with directivity effects). Since this trend is most pronounced for higher frequencies (but still apparent for longer periods), we only focus on PGA, but the results for PSA up to 2 s is provided as an elec. supplement.

Discussion: Understanding the potential causes of (systematic) azimuthal variations in ground motion

The analysis of the within-events residuals of the Silivri Sequence indicate noticeable variation with respect to azimuth, with increasing ground motion amplitudes towards the north-eastern Marmara Region. The majority of GMPEs rely on a simplified assumption of an isotropic case and do not account for the "real" anisotropic case, e.g., of the shear-wave radiation pattern, which can also cause earthquake directivity effects (Kotha et al., 2019). Although previous studies have pointed out the importance of including directivity terms into ground motion prediction equations from small-to-moderate events (Courboulex et al., 2013; Chen et al., 2014), there is no available directivity model yet that accounts for earthquake directivity for $M_W \leq 5.8$ events. The extensive study undertaken by the NGA-W2 directivity project (Spudich et al., 2014) provides five different directivity models that can be implemented as an additive term into available GMPEs for magnitudes larger than M_W 5.8. Although the modellers were aware of the fact that directivity can also be present for PGA and PGV and magnitudes down to M 3-5, the lack of small-to-moderate sized events in the near-fault (<70 km) area was the reason that such events were not accommodated (Bozorgnia et al., 2014; Spudich and Chiou, 2008). Physics-based simulations capture well earthquake directivity effects but are mostly based on kinematic models that assume for small earthquake sources a simple radially symmetric rupture and ignore possible complex rupture processes as well as variable rupture velocity (Kane et al., 2013). Karabulut et al. (2021) confirms the complex behavior of the moderate M_W 5.8, 2019 Silivri event with increasing rupture velocity and slip values (100 cm) towards the east. The rupture of the mainshock was found to be larger towards the east (5 km) than towards the west (3 km). Our results of higher ground motion values towards Eastern Marmara therefore further support the results of Karabulut et al. (2021), who proposed a dominant rupture propagation towards the east coupled with eastward directivity effects for the broken fault segment of the MMF. This hypothesis needs to be explored, however, and in the following, we address in turn each of the potential site-, path-, and source effects that may have led to the observed azimuthal ground motion variations.

Site-effects

The selected ground motion models predict ground-shaking with at least one site-descriptor parameter included (v_{S30}). The NGA-W2 models CY14 and BSSA14 have an additional site term, $z_{1.0}$, a proxy for seismic basin depth defined as the depth at which the shear-wave velocity reaches 1.0 km/s. For the stations considered in this work, in terms of measured v_{S30}, the stations are equally distributed with the majority belonging to the EC8 site classes B and C (Figure 1). This agrees with the dataset of the Bi14 model which was derived using mainly Turkish recordings, as the majority of stations belonging to these site classes. Furthermore, the residual analysis considering the v_{S30} predictor variable (Figure 4, bottom two rows) already indicated no relationship between the predicted residuals and v_{S30}. However, v_{S30} and $z_{1.0}$ describe site terms in a simplified manner. Local geological site-conditions and the characteristics of the basin sub-surface topography may amplify (or even de-amplify) earthquake ground motions significantly. If the observed trend in azimuthal variations of ground motions arose due to possible geological effects (site effects) and not because of the earthquake source or travel path effects, the trend of higher values towards the Eastern Marmara should be evident for other earthquakes in the nearby region. We assess whether this is likely to be the case by exploring the within-event residuals for another recent event in the Marmara Region that is not located on the MMF. Accordingly, the onshore M_W 4.1, 25/06/2016 event close to the city of Yalova was selected. Figure 5d shows the difference in ground motion residuals calculated for the M_W 5.8 Silivri and M_W 4.1 Yalova events using the Bi14 GMPE for PGA. Since the Yalova event occurred onshore, the vast majority of stations are located in Eastern

Marmara and stations towards the western portion of the Marmara Region are missing. These results show that residuals from the two events are substantially different from each other, hence, we suggest that there is no systematic influence of site effects on the resulting ground motion. Another non-reference site technique is the evaluation of the horizontal-to-vertical (also called H/V) spectral ratios. The deconvolution of the vertical component from the horizontal leads to an approximate representation of site-response. To calculate the event-specific H/V ratios, a 5%-cosine taper has been applied to the time series and the corresponding Fourier amplitude spectra of all three components have been smoothed using the Konno-Ohmachi smoothing algorithm with a bandwidth, b, of 40. Two stations were selected for this analysis (Figure 6): AFAD station codes 4121 and 1710. The first station is in the direction of rupture propagation, east of the epicenter and the second located in the backward direction of the rupture propagation, west of the epicenter. These sites will be referred to from now as the directive and anti-directive sites, respectively, according to Somerville et al. (1996). These two sites were selected since they are characterized by almost identical v_{S30} profiles of 283 m/s (station 1710) and 286 m/s (station 4121) and similar R_{jb}, but significantly different PGA values (PGA_{1710} = 1.78 cm/s^2 ; PGA_{4121} = 10.72 cm/s^2).

[Figure 6 here]

Figure 7 shows the mean horizontal-to-vertical (H/V) spectral ratios for the two selected stations (Figure 6, black triangles) using recordings of the Silivri Sequence. The most energetic S waves (e.g., 0.1 to 10 Hz) show similar H/V ratios for both stations. Peak frequencies in the H/V ratios are at 0.1-0.2 Hz (i.e., at long periods of 5-10 seconds) for both sites. While H/V spectral ratios of earthquakes can be considered to provide only a lower bound of the absolute amplification, the similarity of the spectral ratios from all events indicates that site effects only play a minor role over the entire frequency range and would not account for the ground-motion differences observed between these two stations.

[Figure 7 here]

Path-effects

Due to the limited number of earthquakes considered in this study, path-effects could not be evaluated empirically, but were instead interpreted with reference to the local bedrock geology and to previous studies of crustal structure that are based on numerical simulations. The Marmara Region is marked by different geological formations with significant stratigraphic variability that could have a large influence on seismic wave propagation. To the north-west, the region is surrounded by the Thrace Basin formation, which is primarily composed of Quaternary to Tertiary basins. The Eastern Marmara, by contrast, is dominated by comparatively older Cretaceous formations (Ergün and Özel, 1995). While seismic attenuation is dependent on many factors, previous studies have demonstrated that it is strongly sensitive to temperature, structure, and the presence of fluid phases within the Earth (Solomon, 1972; Wu et al., 2007). Geothermal areas, such as those present in the Armutlu Peninsula in the Eastern Marmara are therefore suggested to represent strong seismic attenuation. Zhao and Xie (2016) have demonstrated high Q_{LG} anomalies for that region (Q_{LG} = attenuation quality factor measured from the Lg-coda), whereby the western portion of the Marmara Sea is represented by lower Q_{LG} anomalies. Indeed, these crustal anomalies could explain the azimuthal dependence of ground motion amplitudes, which are higher towards the Eastern Marmara. However, one of the major outcomes of their study was the frequency-dependency of their proposed broadband Lg-wave attenuation models, with higher attenuation anomalies observed at higher frequencies. In contrast, our results show that the azimuthal dependency of ground motion amplitudes is persistent even at lower frequencies (see elec. supplement). The travel path of seismic waves is further controlled by heterogeneities in crustal velocity and attenuation. Many studies have described the Marmara Region's velocity structure, with several discrepancies arising between these works. For example, Baris et al. (2005) found that based on travel time data, there are strong lateral heterogeneities in the eastern Marmara Region. Koulakov et al. (2010) observed a low shear wave velocity (V_S) structure beneath the Adapazari Basin and high velocities (low attenuation) around the Kocaeli/Armutlu region. A more recent study by Polat et al. (2016) based on local earthquake tomography demonstrated that the seismic velocity distribution is consistent with the tectonic features of the Marmara Region. Accordingly, at shallow crustal depths (5-15 km), high P- and S-wave velocities are present beneath the Armutlu Peninsula and Yalova. In summary, we cannot necessarily preclude the possible influence of path effects on the observed azimuthal variability in ground motions. However, from the many lines of investigation that we have explored through various geophysical studies found in the literature, we cannot find a clear and coherent physical explanation for all of the spatial trends we are observing in the residuals across a range of frequencies. This issue should then remain open as a point of future discussion and analysis.

Source-effects and implication of rupture directivity

The two stations that were discussed previously (Figure 6) are now used to analyze earthquake directivity effects in the ground motion discussed by Karabulut et al. (2021). Figure 8 shows in the first row the acceleration recordings of the selected directive and anti-directive sites. The first noticeable difference between the two stations is the maximum amplitude of the directive station, which is almost a factor of 5 larger than the maximum amplitude of the anti-directive site. Also, the respective fault normal (FN) and fault parallel (FP) components of the directive station (right plot Figure 8) show major differences in their amplitudes, with a larger maximum on the FN component. This is a classic observation associated with directivity-effects and can be explained by the fact that for strike-slip faulting mechanisms (such as was the case for the M_W 5.8 and M_W 4.1 events in the Silivri Sequence) the S-wave radiation pattern maximum is in the strike-normal (e.g., FN) direction, whereas the strike-parallel will be marked by lower amplitudes (Somerville et al., 1997; Bray and Rodriguez-Marek, 2004; Chiarabba et al., 2009; Kotha et al., 2019).

[Figure 8 here]

Directivity results when the rupture velocity exceeds or is close to the shear-wave velocity. Accordingly, a station located towards the rupture front (i.e., a directive site) will experience a pulse-like motion at the beginning of the recording (Somerville et al., 1997; Bray and Rodriguez-Marek, 2004; Baker, 2007). Recent studies made on NGA-W2 (Bozorgnia et al., 2014) data have generally modelled directivity as a narrow-band phenomenon, usually affecting a limited period range that depends on the magnitude of the events (typically with T > 1s for earthquakes with magnitude greater than M 5). This effect can be seen more clearly in the velocity or displacement time histories. Figure 8 bottom row confirms the appearance of a pulse-like motion in the velocity-time domain for the directive station. The PGV values are too low (PGV < 30 cm/s) to be quantified as a pulse motion according to the classification of Baker (2007), but this feature is apparent for other stations located in the rupture direction, so we will continue to refer to it as "pulse-like" due to its appearance. This pulse-like motion, however, occurs at an intermediate point of the recording (around 20 seconds after the onset of the S-wave) at a distance of approximately 100 km. This observation is consistent with the previous detection of directivity effects at large distances for even smaller events of M_W< 7 (Courboulex et al., 2013; Chen et al., 2014). In comparison, the anti-directive site shows significantly lower amplitudes and no indication of a pulse-like motion. Figure 9 shows the pseudo-spectral-velocity (PSV) for the directive and anti-directive stations, where the peaks for the directive site are around 2-3 s. The anti-directive sites represented by red curves show noticeably lower PSV values than the directive sites. The maximum spectral values are 5-15 times larger for the directive sites, compared to the anti-directive sites.

[Figure 9 here]

The directivity effects suggested by these observations cannot, however, be easily compared with existing ground-motion models that have integrated directivity models. Indeed, the NGA-West Directivity group has provided an extensive study (Spudich et al., 2014) that proposed five different directivity models intended for application in seismic hazard analysis. While it is acknowledged that directivity can occur at distances larger than 100 km and from smaller events, hence, none of the proposed models are applicable for the present distance and magnitude range. For example, the CY14 model based on the direct point parameter (DPP) predicts significant directivity effects at shorter distances (< 70 km) and for larger magnitude earthquakes (M_W > 5.7). Only one of three selected events fall within this magnitude range and from this only a few records fall within this distance range, the expected amplification due to the directivity would be minimal. Accordingly, the application of

CY14 while including the directivity term would still predict levels of ground motion that are not consistent with the observations made in this study. Our observations are intriguing, however, since they indicate that the major earthquakes of the Silivri Sequence have all been mostly unilateral with ruptures systematically propagating from west to east. The assumption of systematic directivity effects agrees with the observations proposed by Karabulut et al. (2021) who indicated an 8 km extending eastward directivity with increasing shear-wave velocities from west to east.

This raises the question of whether future and larger earthquakes on the MMF would also rupture towards the east. Ben-Zion and Andrews (1998) and Ben-Zion and Sammis (2003) provided a theoretical background for such a hypothesis. According to these studies, a sharp material contrast on a strike-slip fault will lead to asymmetric motion on different sides of the rupture and thus to a preferred rupture propagation direction. Meanwhile, Le Pichon et al. (2003) concluded that geological rock properties are different on both sides of the Main Marmara fault (creeping and locked sections), demonstrating the existence of asymmetric elastic loading along the MMF.

Conclusions

This study investigated the regional variability of the strong ground motion recordings of the largest three events in the Silivri Sequence: the M_W 5.8 and M_W 4.1 events that occurred on 26 September 2019, and the M_W 4.7 event that followed on

11 January 2020. Their between-event residuals (δ_{Be}) and within-event residuals ($\delta_{W,es}$) were analyzed to interpret the implications regarding the impact of source effects and path propagation on the regional variability in observed ground-motion amplitudes. Our results show clear azimuthal trends in ground motion, even at larger epicentral distances (up to 100 km) for PGA and a wide range of spectral periods, which are not captured by recent GMPEs. Higher ground motions are observed towards the Eastern Marmara, Armutlu Peninsula, and Kocaeli. Our results are supported by the study of Karabulut et al. (2021), who proposed eastward directivity effects along the MMF that are aligned with the rupture propagation. Since the increasing trend of higher ground motion residuals is persistent for all three events on the MMF, we assume systematic rupture directivity which may be caused by the sharp material contrast across the fault. Our results highlight the importance of including source-related effects (radiation patterns and directivity effects) to predict the azimuthal variations of moderate earthquakes ground motion. This study also suggests the interest of systematically and globally studying the directivity of moderate earthquakes to evaluate the systematic character of the rupture direction, especially for large strike-slip faults showing sharp material contrasts.

References

Akkar, S., Sandıkkaya, M. A., Şenyurt, M., Sisi, A. A., Ay, B. Ö., Traversa, P., Douglas, J., Cotton, F., Luci, L., Hernandez, B., and Godey, S. (2014). Reference database for seismic ground-motion in Europe (RESORCE), Bull Earthq Eng 12(1) 311-339

Al Atik, L., Abrahamson, N., Bommer, J. J., Scherbaum, F., Cotton, F., and Kuehn, N. (2010). The variability of ground-motion prediction models and its components, Seismol Res Lett 81(5) 794-801

Ambraseys, N. N., Douglas, J., Sarma, S. K., and Smit, P. M. (2005). Equations for the estimation of strong ground motions from shallow crustal earthquakes using data from Europe and the Middle East: horizontal peak ground acceleration and spectral acceleration, Bull Earthquake Eng 3(1) 1-53

Baker, J. W. (2007). Measuring bias in structural response caused by ground motion scaling, Pacific Conf Earthq Eng, no. 056, 1–6, doi: 10.1002/eqe

Baris, S., Nakajima, J., Hasegawa, A., Honkura, Y., Ito, A., and Üçer, S. B. (2005). Three-dimensional structure of Vp, Vs and Vp/Vs in the upper crust of the Marmara region, NW Turkey, Earth Planets Space 57(11) 1019-1038

Bates, D., Kliegl, R., Vasishth, S., & Baayen, H. (2015). Parsimonious mixed models. arXiv preprint arXiv:1506.04967.

Ben-Zion, Y., and Andrews, D. J. (1998). Properties and implications of dynamic rupture along a material interface, Bull Seismol Soc Am 88(4) 1085-1094

Ben-Zion, Y., and Sammis, C. G. (2003). Characterization of fault zones, Pure Appl

Geophys 160(3) 677-715

Bindi, D., Massa, M., Luzi, L., Ameri, G., Pacor, F., Puglia, R., and Augliera, P. (2014). Pan-European ground-motion prediction equations for the average horizontal component of PGA, PGV, and 5%-damped PSA at spectral periods up to 3.0 s using the RESORCE dataset, Bull Earthq Eng 12(1) 391-430

Bindi, D., Picozzi, M., Spallarossa, D., Cotton, F., and Kotha, S. R. (2019). Impact of magnitude selection on aleatory variability associated with ground-motion prediction equations: Part II—analysis of the between-event distribution in central Italy, Bull Seismol Soc Am 109(1) 251-262

Bohnhoff, M., Bulut, F., Dresen, G., Malin, P. E., Eken, T., and Aktar, M. (2013). An earthquake gap south of Istanbul, Nat Comm 4(1) 1-6

Bohnhoff, M., Wollin, C., Domigall, D., Küperkoch, L., Martínez-Garzón, P., Kwiatek, G., Martínez-Garzón, P., Kwiatek, G., Dresen, G., and Malin, P. E. (2017). Repeating Marmara Sea earthquakes: indication for fault creep, Geophys J Int 210(1) 332-339

Bommer, J. J., Douglas, J., Scherbaum, F., Cotton, F., Bungum, H., and Fäh, D. (2010). On the selection of ground-motion prediction equations for seismic hazard, Seismol Res Lett 81(5) 783–793.

Boore, D. M., Stewart, J. P., Seyhan, E., and Atkinson, G. M. (2014). NGA-West2 equations for predicting PGA, PGV, and 5% damped PSA for shallow crustal earthquakes, Earthq Spectra 30(3) 1057-1085

Bozorgnia, Y., Abrahamson, N. A., Atik, L. A., Ancheta, T. D., Atkinson, G. M.Baker,

J. W., Baltay, A. S., Boore, D. M., Campbell, K. W., Chiou, B. S. J., Darragh, R. B., Day, S., Donahue, J., Graves, R. W., Gregor, N., Hanks, T. C., Idriss, I. M.,Kamai, R., Kishida, T., Kottke, A., Mahin, S. A., Rezaeian, S., Rowshandel, B., Seyhan,E., Shahi, S., Shantz, T., Silva, W., Spudich, P. A., Stewart, J. P., Watson-Lamprey, J., Wooddell, K., and Youngs, R. (2014). NGA-West2 research project, Earthq Spectra 30(3) 973-987

Bray, J. D., and Rodriguez-Marek, A. (2004). Characterization of forward-directivity ground motions in the near-fault region, Soil Dyn Earthq Eng 24(11) 815-828.

Chen, Y., Letort, J., Cotton, F., and Drouet, S. (2014). High-frequency directivity effects: evidence from analysis of the Les Saintes records, J Seismol 18(3) 457-466

Chiarabba, C., Amato, A., Anselmi, M., Baccheschi, P., Bianchi, I., Cattaneo, M., Cecere, G., Chiaraluce, L., Ciaccio, M. G., De Gori, P., De Luca, G., Di Bona, M., Di Stefano, R., Faenza, L., Govoni, A., Improta, L., Lucente, F. P., Marchetti, A., Margheriti, L., Mele, F., Michelini, A., Monachesi, G., Moretti, M., Pastori, M., Piana Agostinetti, N., Piccinini, D., Roselli, P., Seccia, D., Valoroso, L. (2009). The 2009 L'Aquila (central Italy) M_w6.3 earthquake: main shock and aftershocks, Geophys Res Lett 36(18) L18308

Chiou, B. S. J., & Youngs, R. R. (2014). Update of the Chiou and Youngs NGA model for the average horizontal component of peak ground motion and response spectra. Earthquake Spectra, 30(3), 1117-1153.

Cotton, F., Scherbaum, F., Bommer, J. J., and Bungum, H. (2006). Criteria for selecting and adjusting ground-motion models for specific target regions: Application to central Europe and rock sites, J Seismol 10(2) 137-156

Courboulex, F., Dujardin, A., Vallée, M., Delouis, B., Sira, C., Deschamps, A., Honoré, L., and Thouvenot, F. (2013). High-Frequency Directivity Effect for an Mw 4.1 Earthquake, Widely Felt by the Population in Southeastern France, Bull Seismol Soc Am 103(6) 3347-3353

Durand, V., Bentz, S., Kwiatek, G., Dresen, G., Wollin, C., Heidbach, O., Martinez Garzon, P., Cotton, F., Nurlu, M., and Bohnhoff, M. (2020). A Two-Scale Preparation Phase Preceded an M w 5.8 Earthquake in the Sea of Marmara Offshore Istanbul, Turkey, Seismol Res Lett 91(6) 3139-3147

Erdik, M., Aydinoglu, N., Fahjan, Y., Sesetyan, K., Demircioglu, M., Siyahi, B., Durukal, E., Ozbey, C., Biro, Y., Akman, H., and Yuzugullu, O. (2003). Earthquake risk assessment for Istanbul metropolitan area, Earthq Eng Vib 2(1) 1-23

Ergintav, S., Reilinger, R. E., Çakmak, R., Floyd, M., Cakir, Z., Doğan, U., King, R. W., and Özener, H. (2014). Istanbul's earthquake hot spots: Geodetic constraints on strain accumulation along faults in the Marmara seismic gap, Geophys Res Lett 41(16) 5783-5788

Ergün, M., and Özel, E. (1995). Structural relationship between the Sea of Marmara basin and the North Anatolian Fault Zone, *Terra Nova* **7**(2) 278-288

Hergert, T., and Heidbach, O. (2010). Slip-rate variability and distributed deformation in the Marmara Sea fault system, Nat Geosci 3(2) 132-135

Kale, Ö., Akkar, S., Ansari, A., and Hamzehloo, H. (2015). A ground-motion predictive model for Iran and Turkey for horizontal PGA, PGV, and 5% damped response spectrum: Investigation of possible regional effects, Bull Seismol Soc Am 105(2A) 963-980

Kane, D. L., Shearer, P. M., Goertz-Allmann, B. P., and Vernon, F. L. (2013). Rupture directivity of small earthquakes at Parkfield, J Geophys Res B Solid Earth Planets 118(1) 212-221

Karabulut, H., Güvercin, S. E., Eskiköy, F., Konca, A. Ö., and Ergintav, S. (2021). The moderate size 2019 September Mw 5.8 Silivri earthquake unveils the complexity of the Main Marmara Fault shear zone, Geophys J Int 224(1) 377-388

Kotha, S. R., Cotton, F., and Dino, B. (2019). Empirical Models of Shear-Wave Radiation Pattern Derived from Large Datasets of Ground-Shaking Observations, Sci Rep 9(1) article number 981

Kotha, S. R., Weatherill, G., Bindi, D., and Cotton, F. (2020). A regionally-adaptable ground-motion model for shallow crustal earthquakes in Europe, Bull Earthq Eng 18 4091-4125

Koulakov, I., Bindi, D., Parolai, S., Grosser, H., and Milkereit, C. (2010). Distribution of seismic velocities and attenuation in the crust beneath the North Anatolian Fault (Turkey) from local earthquake tomography, Bull Seismol Soc Am 100(1) 207-224

Le Pichon, X., Chamot-Rooke, N., Rangin, C., and Sengör, A. M. C. (2003). The North Anatolian fault in the sea of Marmara, J Geophys Res B Solid Earth Planets 108(B4) 2179

Murru, M., Akinci, A., Falcone, G., Pucci, S., and Console, R. T. Parsons (2016). M≥ 7 earthquake rupture forecast and time-dependent probability for the sea of Marmara region, Turkey, J Geophys Res B Solid Earth Planets 121 2679–2707

Parsons, T. (2004). Recalculated probability of M≥ 7 earthquakes beneath the Sea of Marmara, Turkey, J Geophys Res B Solid Earth Planets 109(B5) B05304

Polat, G., Özel, N. M., and Koulakov, I. (2016). Investigating P-and S-wave velocity structure beneath the Marmara region (Turkey) and the surrounding area from local earthquake tomography, Earth Planets Space 68(1) 1-14

Scherbaum, F., Schmedes, J., & Cotton, F. (2004). On the conversion of source-to-site distance measures for extended earthquake source models. Bull Seismol Soc Am *94*(3), 1053-1069.

Schmittbuhl, J., Karabulut, H., Lengliné, O., and Bouchon, M. (2016). Long-lasting seismic repeaters in the Central Basin of the Main Marmara fault, Geophys Res Lett 43(18) 9527-9534

Solomon, S. C. (1972). Seismic-wave attenuation and partial melting in the upper mantle of North America, J Geophys Res B Solid Earth Planets 77(8) 1483-1502

Somerville, P., Graves, R. W., and Smith, N. F. (1996). Forward rupture directivity in the Kobe and Northridge earthquakes, and implications for structural engineering, Seismol Res Lett 67(2) 55

Somerville, P. G., Smith, N. F., Graves, R. W., and Abrahamson, N. A. (1997). Modification of empirical strong ground motion attenuation relations to include the amplitude and duration effects of rupture directivity, Seismol Res Lett 68(1)

199-222

Spudich, P., & Chiou, B. S. (2008). Directivity in NGA earthquake ground motions: Analysis using isochrone theory. Earthquake Spectra, 24(1), 279-298.

Spudich, P., Rowshandel, B., Shahi, S. K., Baker, J. W., and Chiou, B. S. J. (2014). Comparison of NGA-West2 directivity models, Earthq Spectra 30(3) 1199-1221

Strasser, F. O., Abrahamson, N. A., and Bommer, J. J. (2009). Sigma: Issues, insights, and challenges, Seismol Res Lett 80(1) 40-56

Wu, Y. M., C. H. Chang, L. Zhao, J. B. H. Shyu, Y. G. Chen, K. Sieh, and J. P. Avouac, (2007). Seismic tomography of Taiwan: Improved constraints from a dense network of strong motion stations, *J Geophys Res Solid Earth* **112**(8) 1–14

Zhao, L. F., and X. B. Xie (2016). Strong Lg-wave attenuation in the Middle East continental collision orogenic belt, *Tectonophysics* **674** 135–146

Data and Resources

Strong ground motion recording used in this study were obtained from the Turkish Accelerometric Database and Analysis System (TADAS) provided by the Disaster and Emergency Management Presidency (AFAD). The residual analysis part is based on the use of the OpenQuake Software and its related packages (GMPE-SMTK; https://github.com/GEMScienceTools/gmpe-smtk). The maps were made using the

Generic Mapping Tools (GMT) version 5.4.3 (https://www.generic-mapping-tools.org).

Declaration of Competing Interests

The authors declare no competing interests

Acknowledgments

The authors of this paper appreciate the online discussions in the early stages of the work with Prof. Dr. Sinan Akkar, Dr. Abdullah Sandikkaya, and Prof. Dr. Eser Cakir, as well as Prof. Dr. Marco Bohnhoff and the Section 4.2 colleagues. The first author is very thankful for the fruitful discussions she personally had with Dr. Oliver Heidbach and also the feedback from Dr. Yen-Shin Chen and Prof. Dr. Tuna Eken. The authors sincerely acknowledge colleagues from AFAD-Ankara for providing seismic waveform data as well as the online meeting with Dr. Murat Nurlu and section colleagues.

Figures and Tables

Fig.1: Earthquake rupture mechanisms of the three earthquakes used in this study. Red beachballs belong to the 1st (M_W 5.8) and 2nd (M_W 4.1 26/09/2019) Silivri sequence. The blue beachball represents the 3rd event (M_W 4.7 11/01/2020). Earthquake faulting mechanisms are obtained from Karabulut et al. (2020). Red bold line represents the Main Marmara Fault, with Central Basin (CB) on the west, Kumburgaz Basin (KB) at the center and Cinarcik Basin (CiB) in the east. The yellow stars represent the epicenter of the events. Recorded PGA (in cm/s^2) for AFAD strong ground motion records of the M_W 5.8 Silivri main shock and respective site classes based on EC8 site classification (Site class A: Rock site, B: Stiff Soil, C: Soft Soil).

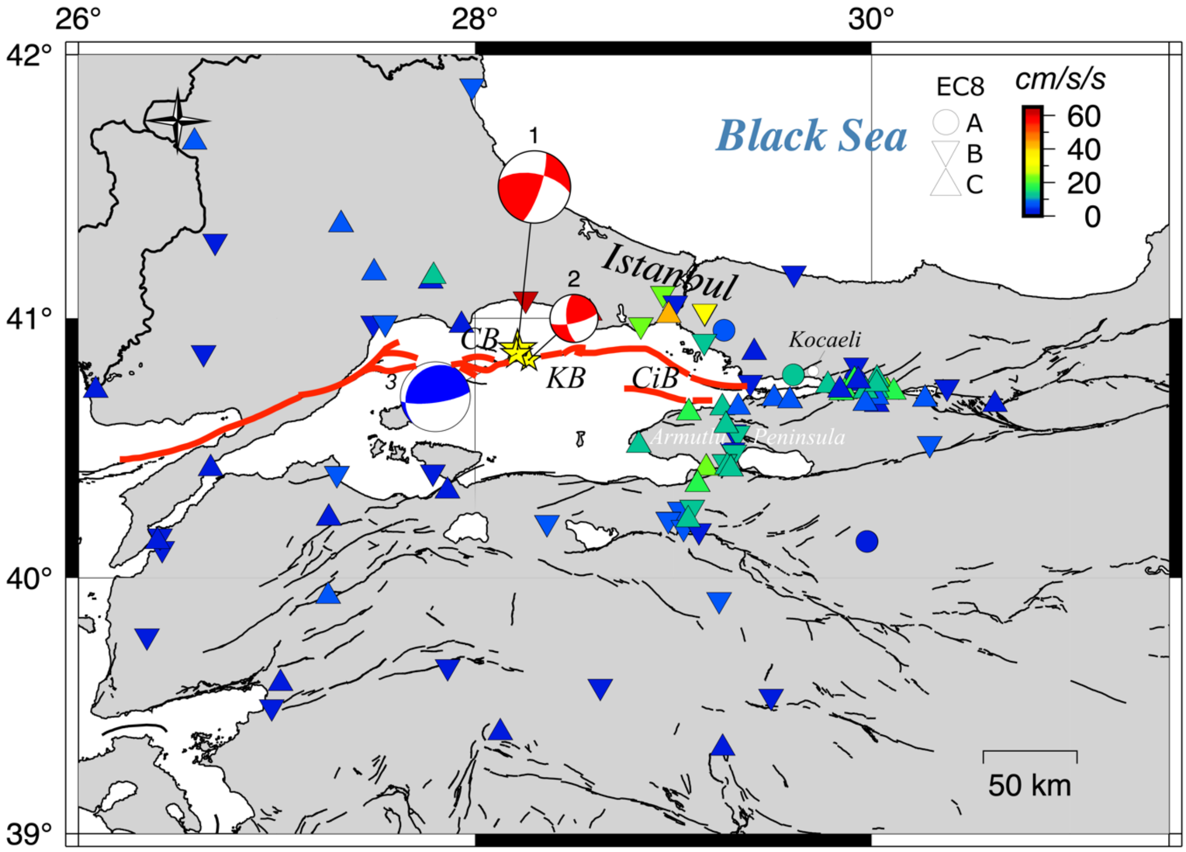

Fig.2: Histogram of within-event residuals for reference GMPEs. The black curve represents the standard normal distribution and the red curve represents normalized observed residuals. The standard deviations and means of the residual analysis are presented in the corner of each plot.

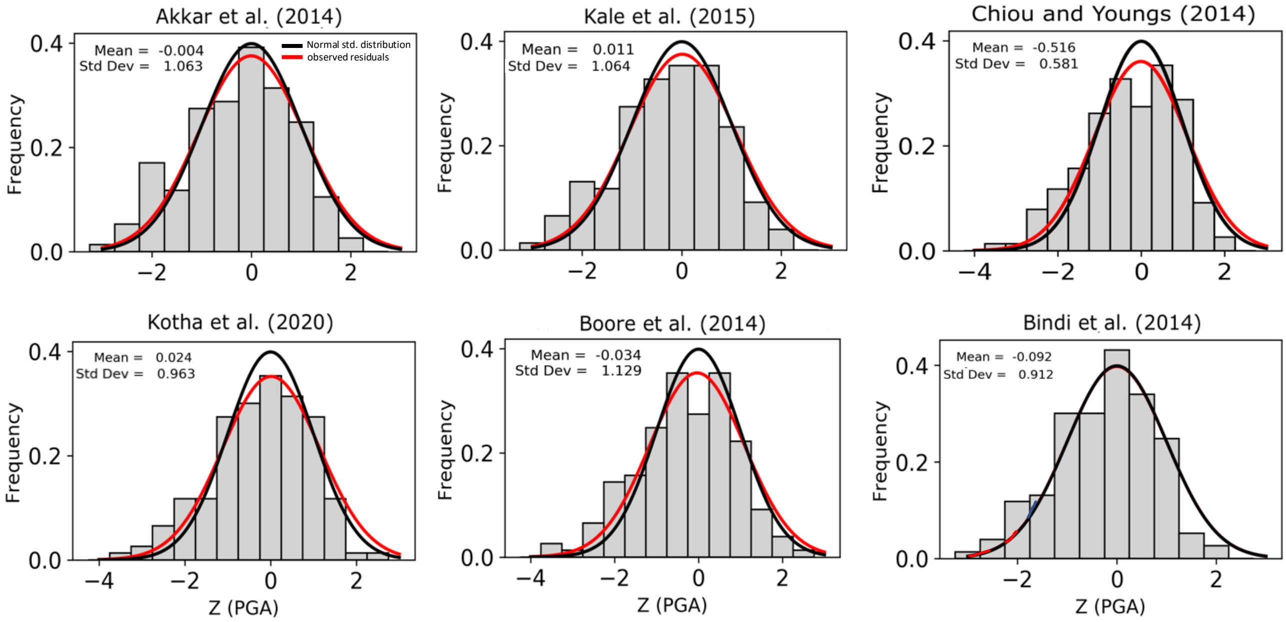

Fig.3: Between-event residuals calculated based on the ground motion prediction equation of Bindi et al. (2014) for the 26th September 2019 10:59 (Event 1), 26th September 2019 M_W4.1 (Event 2), 11:26 and the M_W4.7 11 January 2020 13:36 (Event3) events. The values at 0.01s period correspond to PGA between-event residuals.

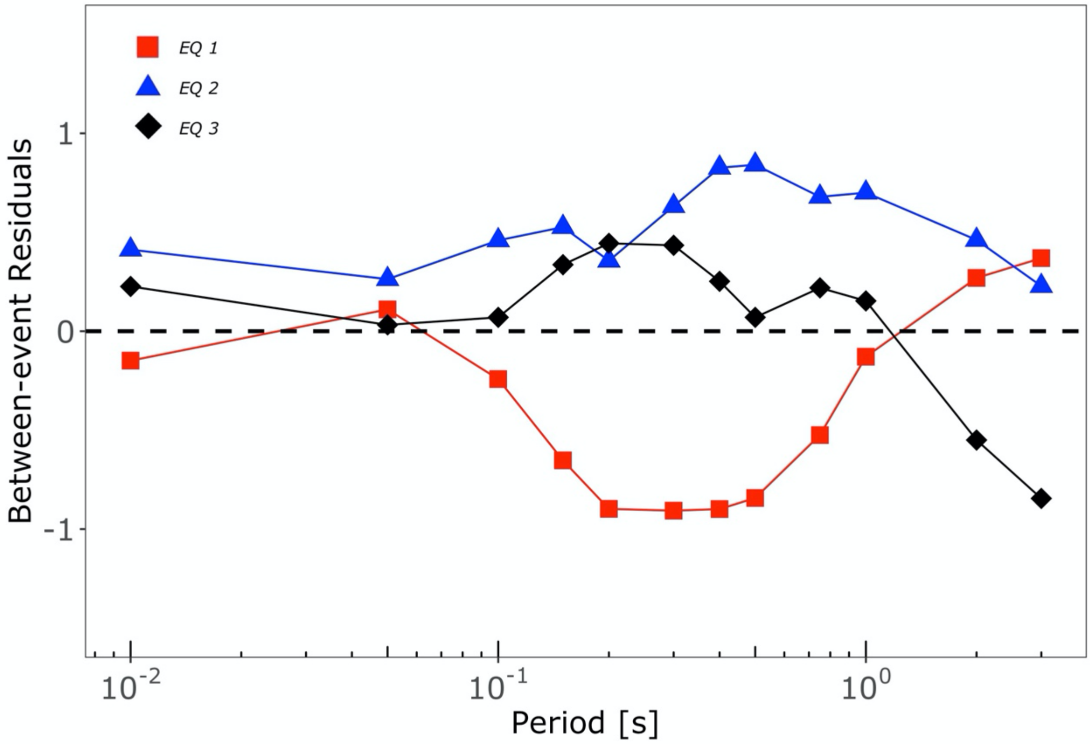

Fig. 4: Distribution of within-event residuals for peak-ground-acceleration (PGA) versus R_{JB}-distance and V_{S30} for all earthquakes that are denoted by different shapes (EQ1: triangle, EQ2: diamonds, EQ3: crosses). The colors indicate the longitudinal position of the stations.

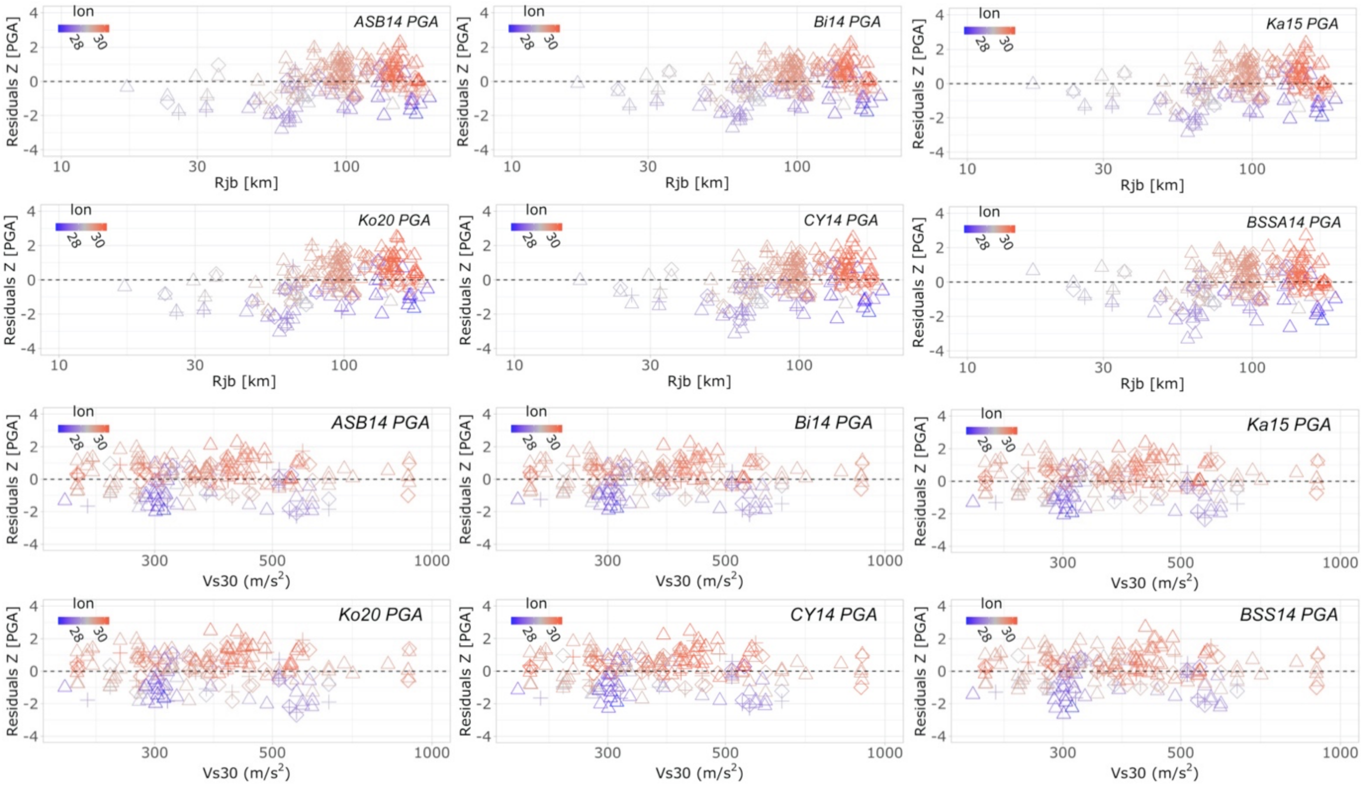

Fig. 5: Spatial distribution of ground motion within-event residuals for the $M_W 5.8$ Silvri sequence, a) $M_W 5.8$, 26th September 2019, 10:56 b) $M_W 4.1$, 26th September, 11:26 c) $M_W 4.7$. 11.01.2020 event d) the residual *difference* between the $M_W 5.8$ Silivri event and $M_W 4.1$ 26.06.2016 Yalova event calculated for PGA using the Bi14 model. Triangles represent the recorded stations with corresponding residuals.

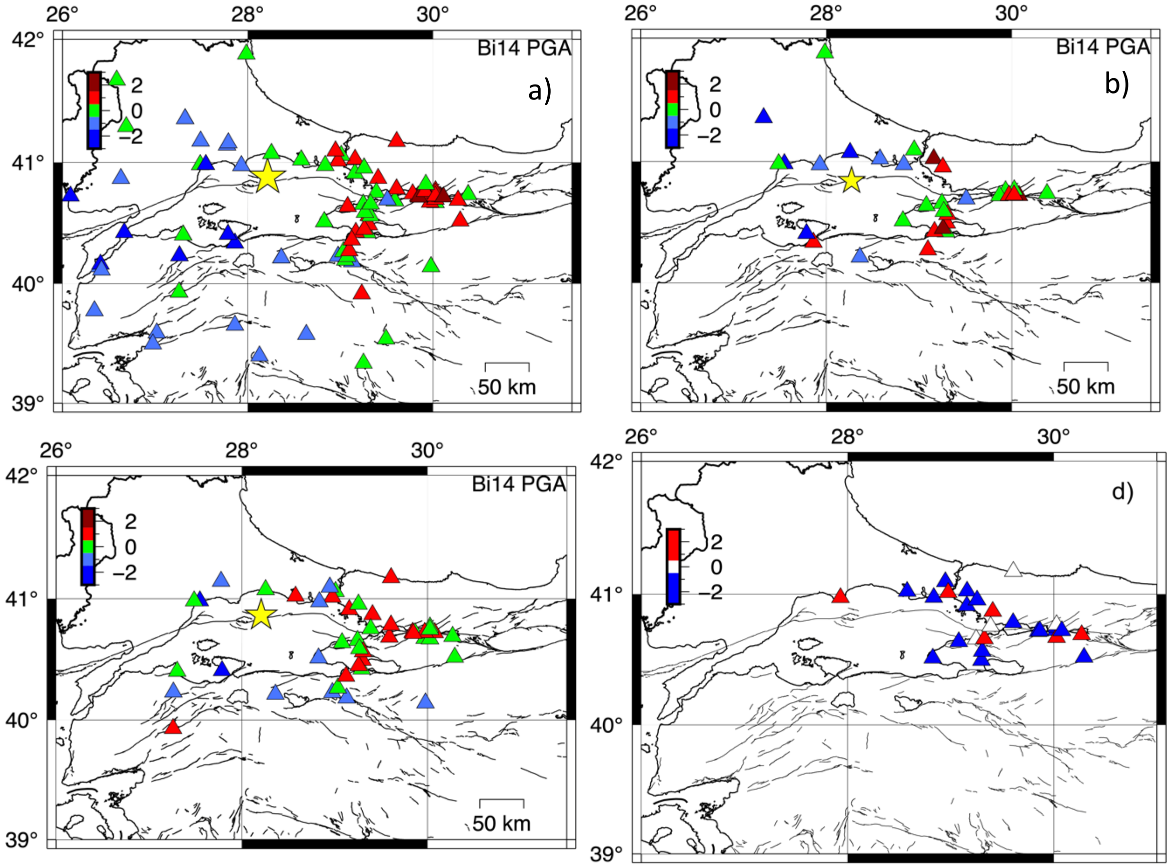

Fig. 6: Selected directive site (station 4121) and anti-directive site (1710) with corresponding recorded PGA values (measured in gravity units) for the 26/09/2019 5.8 M_W mainshock event (black triangles). Red triangles represent the anti-directive (5914, 1715, 1710) and directive stations (4108, 4121, 4129). The site conditions of the two stations are almost identical with a VS30 profile of 283m/s (station 1710) and 286 m/s (station 4121) and epicentral distances of 140 km and 148 km respectively. Yellow stars indicate the epicenters of the three events.

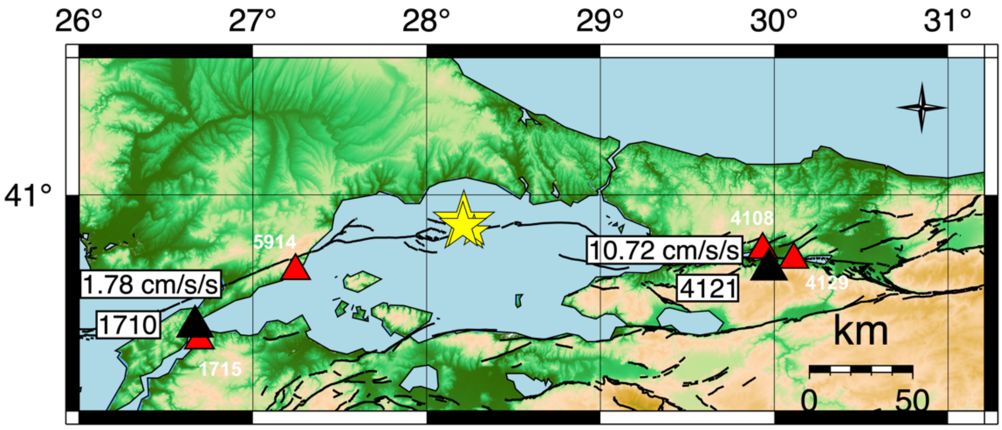

Fig. 7: H/V spectral amplitude ratios of the representative anti-directive (left, station 1710) and directive (right, station 4121) stations. Black curves represent each earthquake recording and red- and blue curves their calculated means.

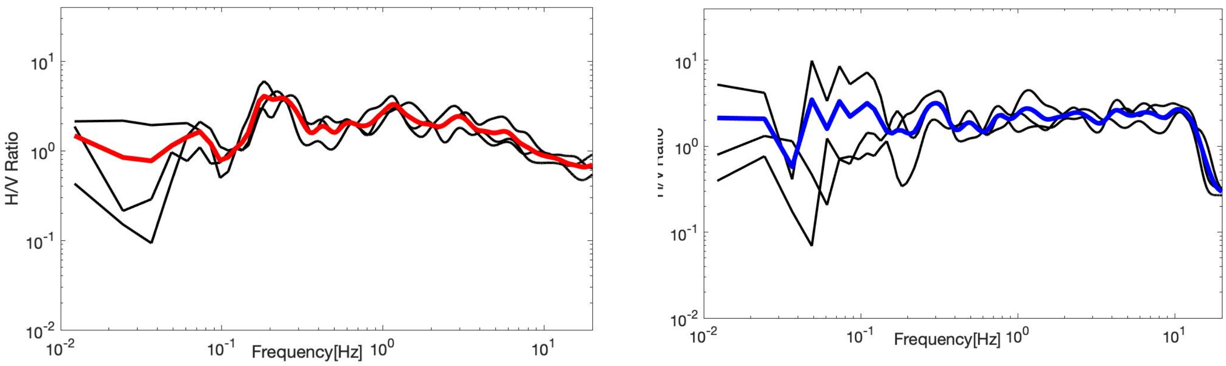

Fig. 8: Acceleration-time recordings of the anti-directive site (1710) and directive site (4121) in the first two rows. Bottom row represents velocity time histories of the two selected stations, respectively. The plots include a cut of recordings at time range of T= 30s - 45s (20s after S-wave onset) demonstrating for station 4121 a pulse-like amplitude.

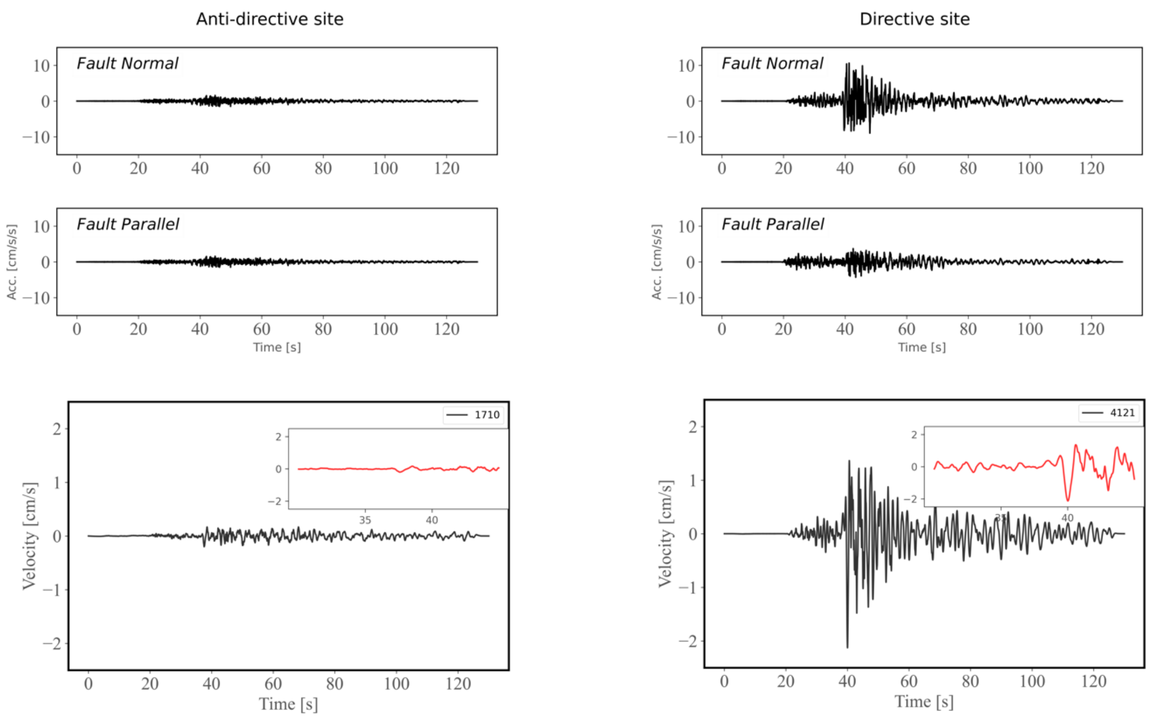

Fig. 9: Pseudo velocity response spectra for N-S component (in cm/s) of selected sites facing the rupture propagation (i.e. directive stations with AFAD station codes: 4121, 4108, 4129) with respect to three stations on the backward of the rupture propagation (i.g. anti-directive sites, station codes: 1710, 1715, 5914).

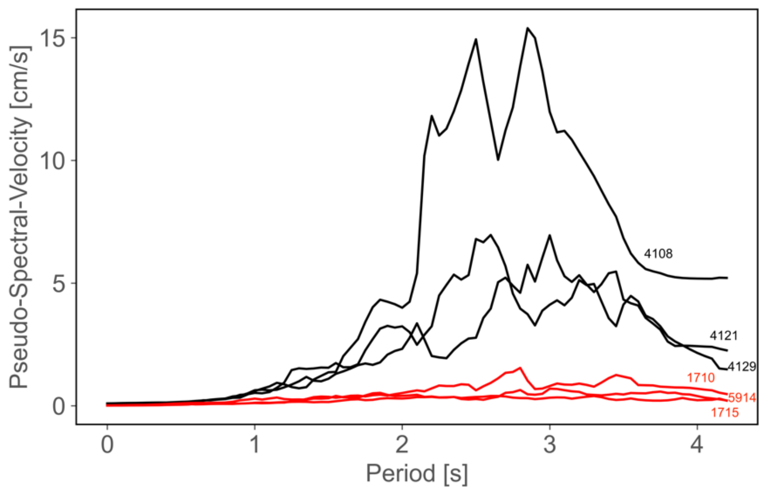

Table 1. Selected Ground Motion Prediction Equations used in this study

Candidate GMPE	GMPE Abbrevation	Magnitude range (M_W)	Period range (s)	Max. Source-to-site Distance (km)	Region of derived Dataset
Bindi et al. (2014)	Bi14	4.0-7.6	0.01	300 (R_{JB})	Europe & Middle East
Akkar et al. (2014)	ASB14	4.0-7.6	0.02– 4.0	200 (R_{JB}, R_{hyp}, R_{epi})	Italy, Turkey, Greece
Kale et al. (2015)	Ka15	4.0-8.0	0.01-4.0	200 (R_{JB})	Turkey and Iran
Kotha et al. (2020)	Ko20	3.0-7.4	0.01-8.0	545 (R_{JB})	Europe
Boore et al. (2014)	BSSA14	3.0-7.9	0.01-10.0	400 (R_{JB})	Global
Chiou and Youngs (2014)	CY14	3.0-8.0	0.01-10.0	100 (R_{Rup})	Global

*R_{JB}, Joyner and Boore distance; R_{hyp}, Hypocentral distance; R_{Rup}, rupture distance, R_{epi}, epicentral distance

Table 2. Event information

No	Event Date	Time	M_W	Depth (km)	No of rec.
1	26.09.2019	10:59	5.8	7.97	32
2	26.09.2019	11:26	4.1	4.58	45
3	11.01.2020	13:37	4.7	10.82	76